https://dx.doi.org/10.1016/j.jsv.2022.116778

A tunable hybrid damper with Coulomb friction and electromagnetic shunt damping

Ruqi Sun, Waion Wong*, Li Cheng
Department of Mechanical Engineering
The Hong Kong Polytechnic University, Hong Kong, PRC

Abstract:

Vibration dampers with tunable properties are of practical significance to accommodate the need of vibration control under different circumstances. Among major parameters, tunable damping to deliver required accuracy within a given frequency range is difficult to achieve in practice. This paper proposes a hybrid tunable damper by combining the advantages of both Coulomb friction damping and electromagnetic shunt damping. The tunable friction damper (FD) allows for coarse tuning with a larger tunable range, while the tunable electromagnetic shunt damper (EMSD) functions as a fine tuner with fine precision. The end result is a significantly increased tunable frequency range with high precision. The proposed method allows for simple and low cost adjustment of the damping forces in both dampers. A prototype is fabricated and experimentally tested in a dynamic vibration absorber (DVA) system. The predicted tenability is experimentally verified and H_∞ optimal damping of the DVA is readily achieved by using the proposed hybrid damper.

Keywords:

Tunable hybrid damper, Coulomb friction damping, Electromagnetic shunt damping, Dynamic vibration absorber

1. Introduction

Tunable damping is much needed in motion control of robots which usually requires low damping during its motion and high damping to prevent oscillation about its target position. Same applies to vibration isolation of machinery and structures which demand large damping during startup to reduce resonant vibration and low damping at its steady operating frequency. Some applications are damping sensitive, exemplified by a dynamic vibration absorber (DVA) which needs to operate with optimum damping to meet the designed performance. However, the commonly used viscous damper can hardly offer the required tunability after being manufactured. On the other hand, magnetorheological (MR) dampers, which can potentially offer tunability and fast response, are not widely applied in industry because of their cost and external power supply requirement. Moreover, both viscous and MR dampers require

* Corresponding author.
E-mail address: mmwowong@polyu.edu.hk (Waion Wong)

proper sealing to prevent leakage of the functioning fluid inside the damper. Alternatively, a piezoelectric shunt damper can provide tunable damping force, mainly applied to thin-wall structures under high-frequency excitations.

As an emerging concept, electromagnetic shunt damper (EMSD) has been exploited for vibration control and energy harvesting since its first inception [1]. Owing to its fine tunability of the generated damping force, EMSD has been implemented in various applications such as vibration isolation of single-degree-of-freedom systems [2-5], dynamic vibration absorbers [6-9], vibration control of cantilever beams and plates [10-12], etc. Various control strategies were also developed, exemplified by passive control [13], adaptive control [14], hybrid control [15], H_∞ and H_2 optimization [16-17] etc. Nonlinear damping was also investigated with a nonlinear EMSD [18-20], for which equivalent nonlinear damping and nonlinear mass were derived and verified with specifically arranged magnets. Moreover, EMSD was shown to entail simultaneous vibration control and energy harvesting [21-24]. However, the application of EMSD is limited to the vibration control of heavy machines or low-frequency problems because of the insufficient damping force provided by EMSD.

Since the damping coefficient of an EMSD is inversely proportional to the circuit resistance, negative impedance was used to improve the tunable damping range [25-27]. However, a negative resistor requires external power supply, which adds system complexities and restricts its applications. The system can even become unstable if the absolute value of the negative impedance is larger than the internal impedance of the EMSD coil. Moreover, the excessive sensitivity of the system to negative impedance is not suitable for the fine-tuning of damping, as to be theoretically illustrated later on in this paper. Therefore, a hybrid damper with a different type of coarse tuning method is needed to alleviate the above shortcomings.

A friction damper (FD) is on the top of the alternatives to provide a large damping force with light and a small structural body. The stick-slip boundary determined by FD was deduced analytically while Den Hartog investigated the forced vibration of a single-degree-of-freedom (SDOF) system with combined viscous and Coulomb damping [28]. The displacement transmissibility in a SDOF system with a FD in either a fixed or oscillating wall was investigated [29], and the corresponding experimental results verified Den Hartog's analytical results [30]. Used as a vehicle semi-active suspension, a tunable FD was modeled and experimentally investigated with an electrohydraulic driving system [31]. The experimental results showed that the residual back-pressure and reduced hydraulic system bandwidth are two significant issues, which can be coped with by a preloading spring and a pressure control loop. Meanwhile, FDs have also been applied to damp cable vibrations [32].

Due to the nonlinearity of the FD, few research was conducted in view of its application as a DVA. H_∞ optimal DVA [33] can be implemented with properly tuned FD in both translational [34] and rotational [35] forms. Particularly, relative to the excitation force, a small dry friction force can function well in a DVA without inducing the stick-slip motion [34-36]. A statistical linearization method was proposed to replace

the nonlinear friction damping with equivalent viscous damping [37]. Moreover, both rigid and flexible friction dampers were theoretically investigated for optimum DVA implementation [38]. Results show that both dampers can obtain the H_∞ optimal status of the DVA, and the flexible friction damper performs better with higher stiffness. This alludes to the possibility of exploiting tunable FD to provide coarse damping tuning for the H_∞ optimal DVA as long as the Coulomb damping force is restricted to avoid the stick-slip motion.

The above literature review suggest that the damping enhancement method specific to EMSD is mainly confined to the use of negative impedance. Meanwhile, the nonlinearity of FD also limits its application in DVAs. To tackle these issues, a tunable hybrid damper with Coulomb friction and electromagnetic shunt damping is proposed in this paper for achieving H_∞ optimal DVA. The damping force in a properly designed FD can be coarsely tuned by changing the normal contact force with a compression spring, and the damping force of the EMSD can be fine-tuned by adjusting the external resistance of the EMSD circuit. The major contributions of this paper are: 1) the tunable damping range is significantly improved by combining a FD and an EMSD of tunable damping forces without compromising the tuning precision; 2) the desired amount of damping can be obtained by a proper combination of the two types of damping; 3) the theoretically predicted H_∞ optimal damping of DVA based on the fixed-point theory is proven experimentally for the first time by using the proposed hybrid damper.

The paper is organized as follows. Section 2 introduces the theoretical model of DVA with hybrid damper, including the mechanism of FD and EMSD. Section 3 provides the procedure of the hybrid damper design and verifies its damping coefficient with experiments. Section 4 presents the on-site experimental calibration of H_∞ optimal DVA with the proposed hybrid damper. Section 5 summarizes the results and conclusions.

2. Theoretical analyses

2.1 Hybrid damper

As the main components of the proposed hybrid damper, EMSD and FD are connected in parallel.

2.1.1 EMSD

A linear EMSD with opposing magnets is adopted as shown in Fig. 1a to fine-tune the damping force [5]. An opposing magnet bar is located in the central hole of the coils, with the adjacent coils connected with 180° phase difference. Electromotive force is induced due to the relative motion between the magnets and the coils. The corresponding damping coefficient c_E can be expressed as:

$$c_E = \frac{K_t^2}{Z} = \frac{K_t^2}{Z_{in} + R_{load}} \tag{1}$$

where K_t denotes the transduction factor; Z the total impedance of the shunt circuit; Z_{in} the impedance of the coil and R_{load} the external resistance of the circuit as shown in Fig. 1b. c_E can be finely tuned by adjusting the external resistance R_{load}.

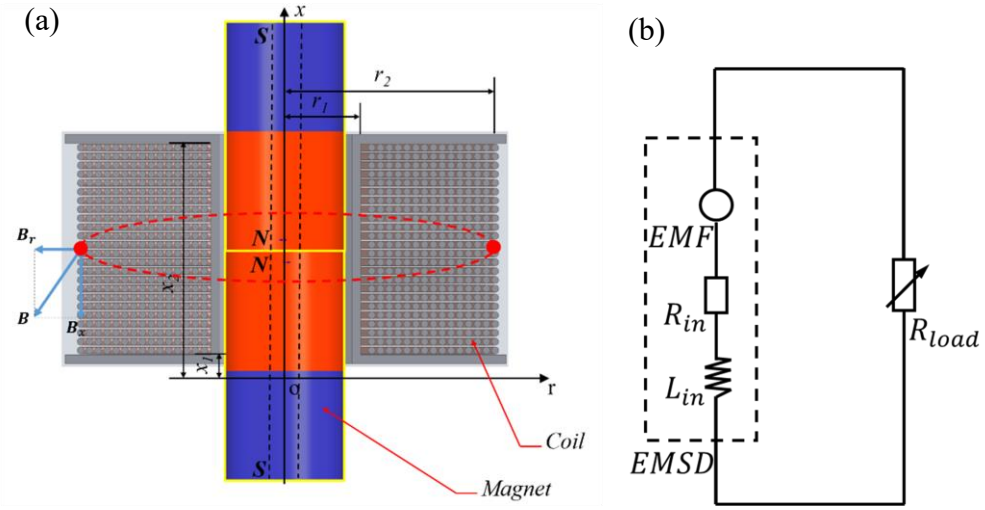

Fig. 1. Linear EMSD with opposing magnet configuration: (a) magnets and coils, (b) shunt circuit

2.1.2 FD

Applying a FD in a SDOF vibration system in Fig. 2, the motion equation of the mass m writes

$$m\ddot{x} + \mu F_N \operatorname{sgn}(\dot{x}) + kx = F_0 \cos \omega t \tag{2}$$

where x denotes the displacement; μ the friction coefficient; F_N the normal force; k the spring stiffness and $F_0 cos\omega t$ the sinusoidal excitation force. $sgn(\dot{x})$ is a signum function defined as

$$\operatorname{sgn}(\dot{x}) = \begin{cases} 1 & x > 0 \\ 0 & x = 0 \\ -1 & x < 0 \end{cases} \tag{3}$$

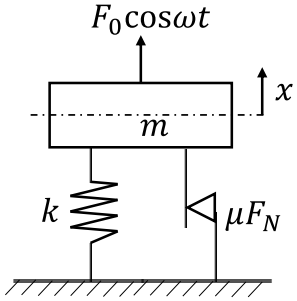

Fig. 2. Schematic of a SDOF system with FD

For a pure Coulomb damper as shown in Fig. 2, the hysteresis loop is a rectangle as illustrated in Fig. 3a. The corresponding energy dissipation ΔE_R per cycle in the damper can be expressed as

$$\Delta E_R = 4\mu F_N X \tag{4}$$

The equivalent damping of the FD can be derived by the energy dissipation per cycle in the hysteresis loop in Fig. 3. The hysteresis loop of a conventional linear viscous damper is an ellipse as shown in Fig. 3b, with the corresponding energy dissipation per cycle ΔE written as

$$\Delta E = \pi c \omega X^2 \tag{5}$$

where c denotes the damping coefficient of linear viscous damping; ω the angular frequency and X the displacement amplitude.

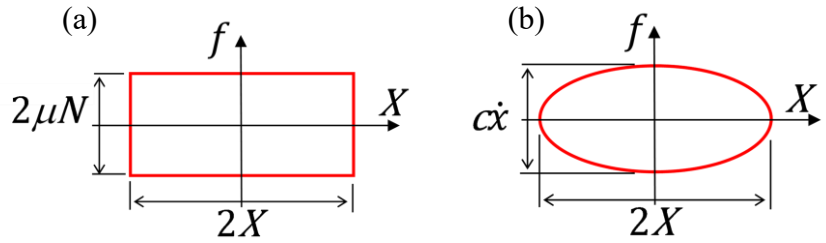

Fig. 3. Hysteresis loop of (a) FD and (b) linear viscous damping

The equivalent damping of the FD can be derived by equating Eqs. (4) and (5), yielding

$$c_R = \frac{4\mu F_N}{\pi \omega X} \tag{6}$$

2.1.3 Hybrid damping

With the EMSD and FD arranged in parallel, the total effective hybrid damping coefficient c can be expressed as

$$c = c_E + c_R + c_P = \frac{K_t^2}{Z} + \frac{4\mu F_N}{\pi \omega X} + c_P \tag{7}$$

where c_P denotes the inevitable parasitic damping in the hybrid damper, which usually can be regarded as a constant Coulomb damping without tunability. Z is the external impedance of the conventional linear EMSD.

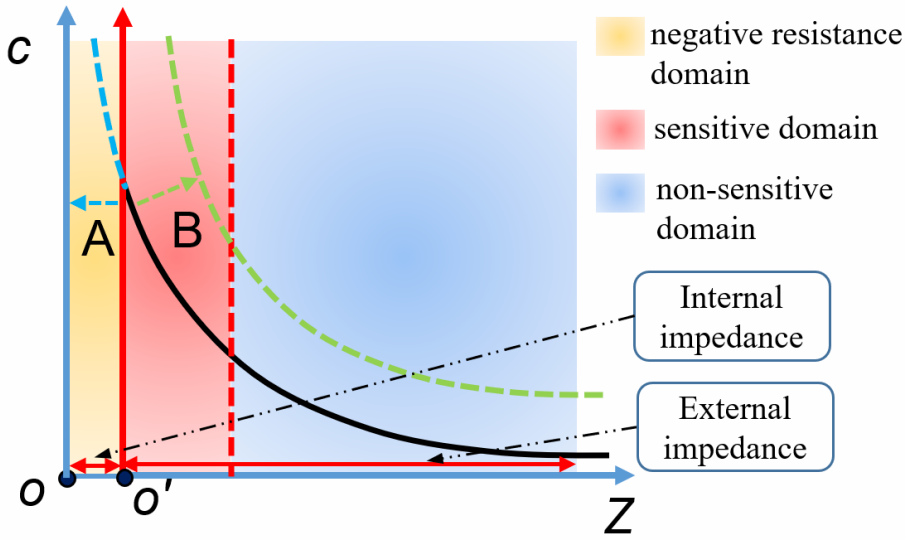

Fig. 4. Total hybrid damping coefficient variation with shunt impedance of EMSD

Given the excitation frequency and response amplitude, the damping coefficient of the FD is regarded as a constant by fixing the normal contact force. Subsequently, the hybrid damping variation with the shunt impedance of EMSD is curved in Fig. 4. The black solid line denotes c variation with Z. Methods A (blue dash line) and B (green dash line) in Fig. 4 correspond to the negative impedance method mentioned above and the proposed hybrid damper, respectively. c varies sharply with the shunt impedance within a sensitive domain. Note that there is no absolute demarcation boundary between the so-called sensitive and non-sensitive domains, they are relative concepts.

As illustrated in Fig. 4, the negative impedance method extends the curve of the conventional linear EMSD by moving the origin coordinate from O' to O. The tunable damping range is increased with negative impedance, but the added region is still located in the sensitive domain where the damping requires precise adjustment of the external impedance. On the other hand, the proposed hybrid damper improves the damping tunability by combining a FD with an EMSD. As illustrated in Fig. 4, the conventional linear EMSD curve is moved up to the green dash line with a constant Coulomb damping coefficient. To achieve the same amount of damping tuning, the proposed hybrid damper is less sensitive to the circuit resistance than the negative impedance method is, thus facilitating the fine-tuning of damping during on-site calibrations of the damper.

2.2 DVA system with hybrid damper

The fine tunability of the proposed hybrid damper is tested on a DVA system which requires optimum damping as shown in Fig. 5. The motion equations of the primary mass m_1 and DVA mass m_2 write

$$m_1\ddot{x}_1 + k_1x_1 + k_2\left(x_1 - x_2\right) + c\left(\dot{x}_1 - \dot{x}_2\right) = F_0\cos\omega t \tag{8}$$

$$m_2\ddot{x}_2 + k_2\left(x_2 - x_1\right) + c\left(\dot{x}_2 - \dot{x}_1\right) = 0 \tag{9}$$

where k_1 and k_2 denote the respective spring stiffness of the primary system and DVA; x_1 and x_2 their respective displacement responses. The respective natural frequency of the primary system and that of the DVA before they are coupled together are $\omega_{n1} = \sqrt{k_1/m_1}$ and $\omega_{n2} = \sqrt{k_2/m_2}$. c is the total equivalent viscous damping coefficient of the DVA provided by the hybrid damper.

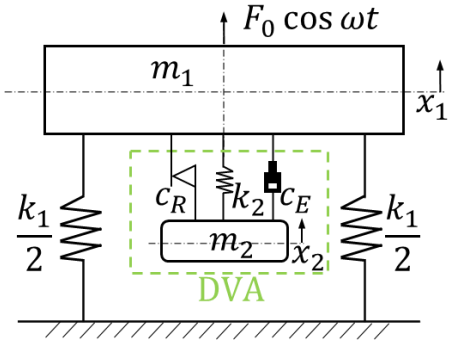

Fig. 5. DVA vibration system with the proposed hybrid damper

The dimensionless displacement response amplitude X_1/X_{st} of the primary system can be derived and written as

$$\frac{X_1}{X_{st}} = \sqrt{\frac{(2\xi\lambda)^2 + (\lambda^2 - \gamma^2)^2}{(2\xi\lambda)^2\left[(1+\mu)\lambda^2 - 1\right]^2 + \left[\mu\gamma^2\lambda^2 - (\lambda^2 - 1)(\lambda^2 - \gamma^2)\right]^2}} \tag{10}$$

where $X_{st} = F_0/k_1$ denoting the static deformation of primary system spring; $\xi = c/c_c$is the damping ratio; $c_c = 2m_2\omega_{n2}$ is the critical damping coefficient of the DVA. $\lambda = \omega/\omega_{n1}$is the frequency ratio; $\gamma = \omega_{n2}/\omega_{n1}$ the natural frequency ratio and $\mu = m_2/m_1$ the mass ratio. The dimensionless displacement response amplitude reaches its min-maximum value with the H_∞ optimal natural frequency ratio and damping ratio.

$$\begin{cases} \gamma_{opti} = \dfrac{1}{1+\mu} \\ \xi_{opti} = \sqrt{\dfrac{3\mu}{8(1+\mu)^3}} \end{cases} \tag{11}$$

The damping coefficient is set to zero to obtain the boundary condition of the stick-slip motion with pure Coulomb damping. Examining the displacement transmissibility from m_1 to m_2 leads to the required range of force ratio, expressed as [29]

$$\frac{F_\mu}{F_k} < \gamma^2 \sqrt{\frac{V^2}{\left(\dfrac{S}{\gamma^2}\right)^2 + U^2}} \tag{12}$$

where $F_\mu = \mu F_N$ is the friction force; $F_k = k_2 X_1$ the equivalent transferred excitation force from the primary system. The dimensionless parameters U, V, S can be

expressed as

$$\begin{cases} U(\gamma) = \dfrac{\sin \pi/\gamma}{\gamma\left(1+\cos \pi/\gamma\right)} \\ V(\gamma) = \dfrac{1}{1-\gamma^2} \\ S(\gamma) = \max\limits_{0\le t\le \frac{\tau}{\omega}} \left[\dfrac{\gamma \sin \omega_{n2} t + U\gamma^2\left(\cos \omega t - \cos \omega_{n2} t\right)}{\sin \omega t} \right] \end{cases} \tag{13}$$

3. Hybrid damper design and analyses

As shown in Fig. 6, the FD and the EMSD are combined and aligned vertically to form a tunable hybrid damper. Since the tuning mechanisms of both components/dampers are fixed together and the moving parts are locked with a coupling mechanism, the Coulomb damping force and the electromagnetic shunt damping force can function on the moving parts simultaneously with independent tunability. Therefore, the two kinds of dampers are connected in parallel conforming to the connection as shown in Fig. 5.

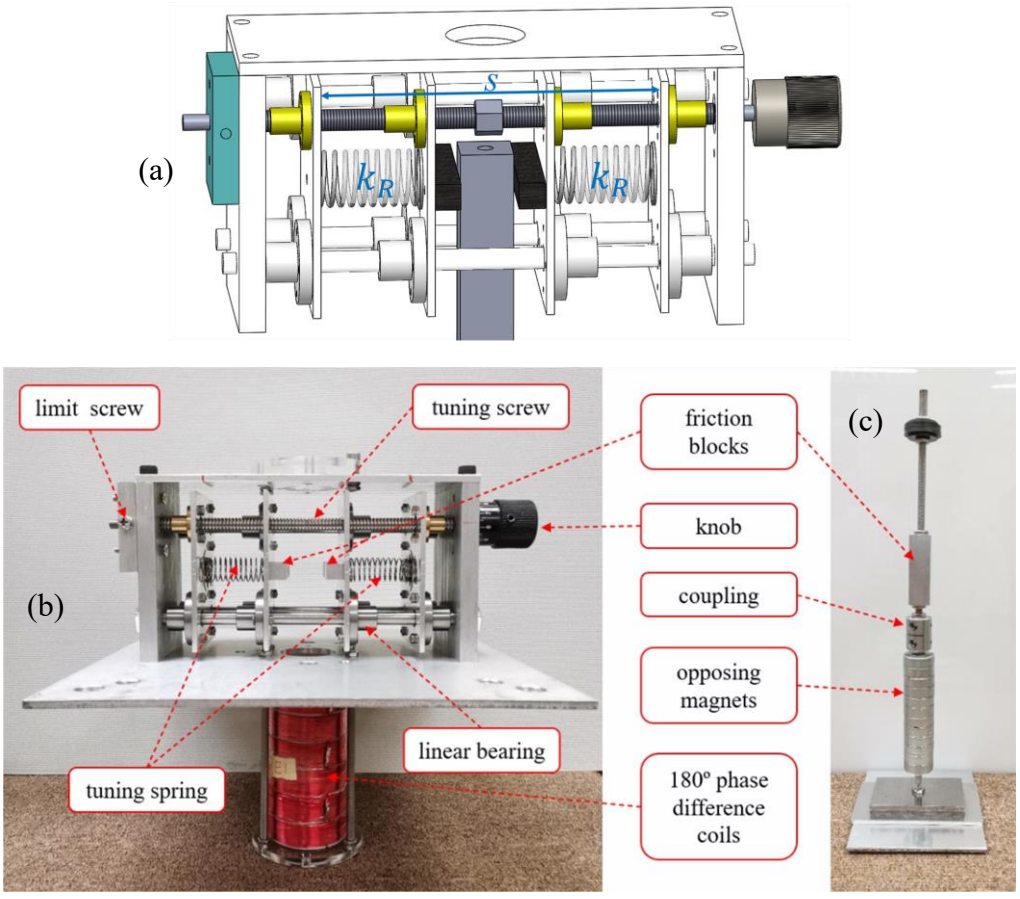

Fig. 6. (a)3D model of FD, and the structure of the proposed tunable hybrid damper, (b) tuning mechanism: tuning spring control part of FD and coils with an external

resistor of EMSD, (c) moving parts: friction block of FD and opposing magnets of EMSD

An opposing magnet configuration of the EMSD [5] is adopted, in light of its verified effectiveness in providing effective damping force. Six opposing permanent magnet pairs and the corresponding coils with 180° phase difference are located on the bottom. The damping coefficient of the EMSD can be adjusted with tunable resistors connected to the coils.

According to Eq.(6), the damping coefficient of the FD can be adjusted by varying the normal force acting on the friction blocks F_N. As shown in Fig. 6b, this force can be varied by adjusting the deformation of the tuning springs with the rotation of the tuning screw. Since the thread of the tuning screw is counter-rotating with levorotatory thread on the left side and dextrorotatory thread on the right side, the varying distance between the copper nuts on the tuning screw is twice as large as the screw pitch of 2 mm per cycle of the screw. Therefore, the total deformation of the tuning springs is 4 mm with one turn of the tuning knob. The damping coefficient can be fine-tuned by precisely controlling the rotation of the knob.

The friction block of the moving part in Fig. 6c is compressed by the symmetrical friction blocks of the tuning mechanism in Fig. 6b. Three smooth shafts and nine linear bearings provide a linear guide to the motion of the nuts on the tuning screw. Moreover, the limit screw on the top-left of Fig. 6b helps fix the rotating angle of the tuning screw.

3.1 Tunable FD

As mentioned above, the adjustable deformation of the tuning springs in Fig. 6b provides the tunable normal force to the friction block of the moving part, leading to the desired damping force in the hybrid damper. As shown in Fig. 6a, the distance s denotes the distance between the farthest left and farthest right nuts on the tuning screw. The deformation of the tuning springs Δs can be defined as

$$\Delta s = s_0 - s \tag{14}$$

where s_0 denotes the initial distance between the friction blocks. The tunable normal force F_N can be expressed as

$$F_N = k_R \Delta s \tag{15}$$

where k_R denotes the stiffness of the tuning springs. Using Eqs. (6) and (15) and eliminating F_N give the equivalent damping coefficient of the FD as

$$c_R = \frac{2\mu k_R}{\pi^2 fX} \Delta s \tag{16}$$

where f denotes the vibration frequency in Hz.

The linear fitting curve of the tuning spring in Fig. 7 shows that the measured stiffness of the spring is around 0.244 N/mm. The friction blocks are made of A356 aluminum alloy, the corresponding friction coefficient locates in the range $\mu \in [0.37, 0.59]$ under different normal forces [39]. Since a soft tuning spring and small tunable range of the normal force are used in the following tests, the friction coefficient μ is assumed to be a constant. The relationship between the absolute value of the FD damping force amplitude F_R and Δs can be expressed as

$$|F_R| = \mu k_R \Delta s \tag{17}$$

Therefore, the product of the friction coefficient and the tuning spring stiffness μk_R can be acquired through the FD hysteresis loop with different Δs.

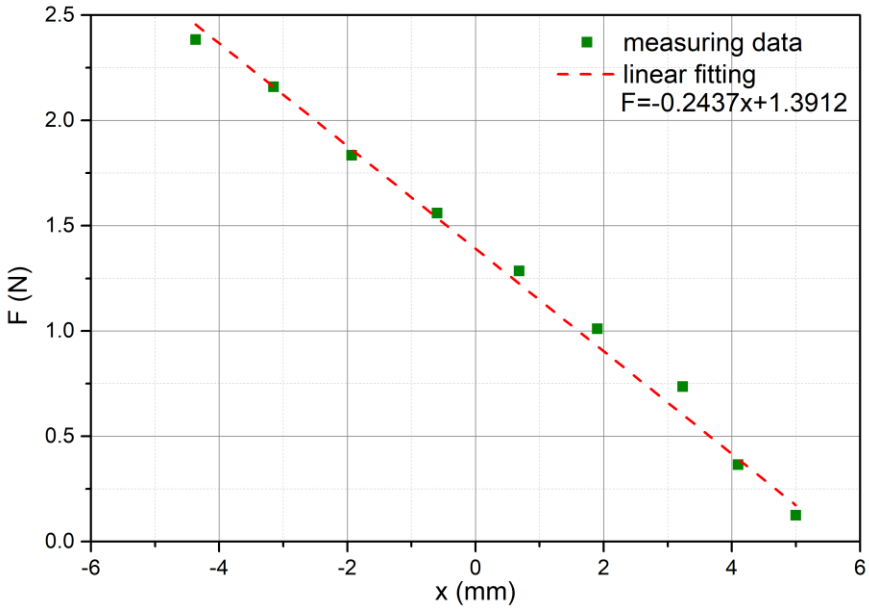

Fig. 7. Tuning spring stiffness test result of FD

3.2 Tunable EMSD

The EMSD in the proposed hybrid damper has six opposing magnet pairs as shown in Fig. 8. The opposing magnet bar locates on the central hole of the coils with coaxial alignment. The air gap between the magnet bar and the inner wall of coils is 2.25 mm to improve the electromechanical coupling efficiency without introducing additional parasitic damping.

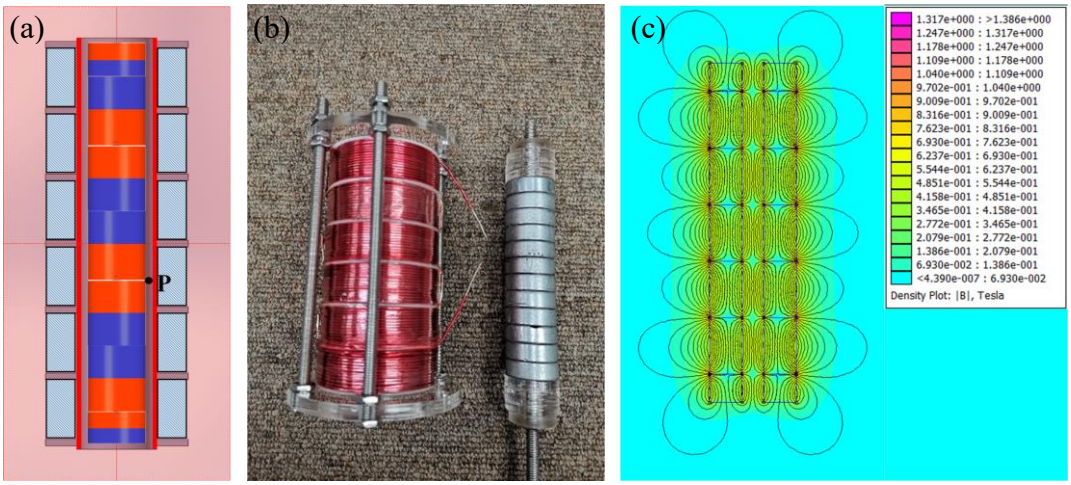

Fig. 8. The proposed EMSD part with opposing magnets configuration: (a) schematic, (b) prototype, (c) magnetic field distribution

$NdFeB$ N33 permanent magnet is chosen as the magnetic field source. The corresponding cloud figure of magnetic flux density is shown in Fig. 8(c). 3D printed nylon skeleton acts as the carrier of the coils to minimize the friction from the magnets bar. A thicker wire diameter ($d_{wire} = 1mm$) of the coil is selected to reduce the heat generation inside the coils. The remaining parameters of the EMSD are listed in Table 1.

Table 1. The parameters of EMSD

Magnet parameters	Type & grade	*NdFeB* N33
	Internal diameter	6 mm
	External diameter	24.5 mm
	Length	8 mm
	Quantity	12
Skeleton parameters	Internal diameter	29 mm
	Thickness	1 mm
	External diameter	50 mm
	Height	98 mm
Coil parameters	Internal diameter(d_1)	31 mm
	External diameter(d_2)	50 mm
	Total length(l_c)	90 mm
	Turns(N_{total})	810
	Wire diameter(d_{wire})	1 mm
	Wire length(L_{wire})	101.8 m

According to Eq. (1), the damping coefficient of the EMSD can be obtained after the determination of the transduction factor K_t and the coil internal impedance Z_{in}.

3.2.1 The transduction factor

The definition of the transduction factor K_t is the path integral of the radial magnetic flux density B_r through the circular coil

$$K_t = -\oint_{loop} B_r(x,r)\,dl \tag{18}$$

For the EMSD with six opposing magnet pairs in Fig. 8, K_t is converted to

$$K_t = -2\pi \sum_{j=1}^{M_a} \sum_{i=1}^{N} r(i,j)\, B_r(x,r,i,j) \tag{19}$$

where M_a denotes the number of opposing magnet pairs; N the number of turns for each coil and $r(i,j)$ the radius of the target coil.

According to Eq.(19), the value of the transduction factor K_t depends on the distribution of the radial magnetic flux density B_r, the radius $r(i,j)$ and the total number of turns $M_a \times N$ of the coils. While $r(i,j)$ and number of turns of the coil are easy to be determined, B_r is determined from the simulation of the magnetic field distribution through a free magnetic finite element analysis software FEMM.

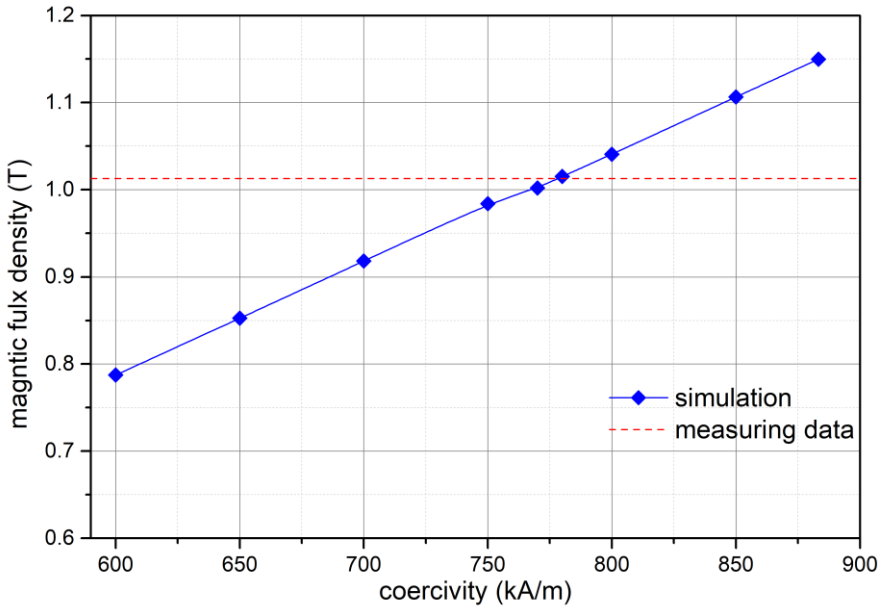

Fig. 9. Simulated magnetic flux density with different coercivity and measured superficial magnetic flux density at target points

The magnet coercivity still requires back derivation with the measured superficial B_r of point P in Fig. 8a. Simulated B_r at point P with different coercivity is shown as the blue dots in Fig. 9. The corresponding measured value is around 1.013T, denoted by the red dash line in the figure. The simulated B_r intersect with the measured value

when the coercivity is around 780kA/m. The corresponding K_t can be calculated as $8.0242\text{V}\cdot\text{s/m}$ with the corrected coercivity based on Eq. (19).

3.2.2 Coil internal impedance

The internal impedance of the coil Z_{in} in Eq.(1) includes the internal resistance R_{in} and inductive impedance $2\pi f L_{in}$ of the coil expressed as

$$Z_{in} = \sqrt{Z_{in}^2 + \left(2\pi f L_{in}\right)^2} \tag{20}$$

where L_{in} represents the coil internal inductance.

The internal inductance is as small as L_{in}=2~3mH, and the hybrid damper works at low-frequency domain. At 10 Hz, for example, the inductive impedance is less than $0.2\,\Omega$ which can be ignored in the internal impedance calculation. Therefore, the internal impedance is approximately equal to the internal resistance

$$R_{in} = \rho \frac{L_{wire}}{S} = \rho \frac{L_{wire}}{\pi\left(d_{wire}/2\right)^2} \tag{21}$$

where $\rho = 0.0175\,\Omega\cdot\text{mm}^2/\text{m}$ denotes the electrical resistivity of copper. With the parameters tabulated in Table 1, the internal resistance is calculated as 2.268 Ω. The measured internal resistance is around 2.250 Ω. The difference between the calculated and measured results is in a reasonable range. Considering the resistance of the connection wires between the coils and the tunable resistor, the value of the total internal impedance is taken as 2.6 Ω. The maximum damping coefficient of EMSD is evaluated based on Eq.(1) ($c_E = 24.765\,\text{N}\cdot\text{s/m}$) when the external resistance R_{load} is zero with the calculated values of K_t and Z_{in} above.

3.3 Damping measurement and verification

The theoretically predicted damping coefficient of the EMSD and the FD with the structural parameters mentioned above can be obtained through Eqs. (1) and (16). For verification purposes, experiments are conducted to deduce the damping coefficients from the measured hysteresis loops in different cases. As shown in Fig. 10, the hysteresis loops can be drawn by the measured damping force and the corresponding displacement with 10 Hz and 1 mm amplitude excitation. The damping coefficient of the energy lost per cycle can then be obtained by

$$c = \frac{\Delta U}{\pi\omega X} = \frac{U_1 - U_0}{2\pi^2 f X} \tag{22}$$

where ΔU is the energy loss, which can be evaluated by the enclosed area of the hysteretic loop. U_1 denotes the energy lost per cycle of the damper at certain deformation of the compression springs of FD (Fig. 10a) or external resistance of EMSD circuit (Fig. 10b). U_0 denotes the energy loss without FD or EMSD.

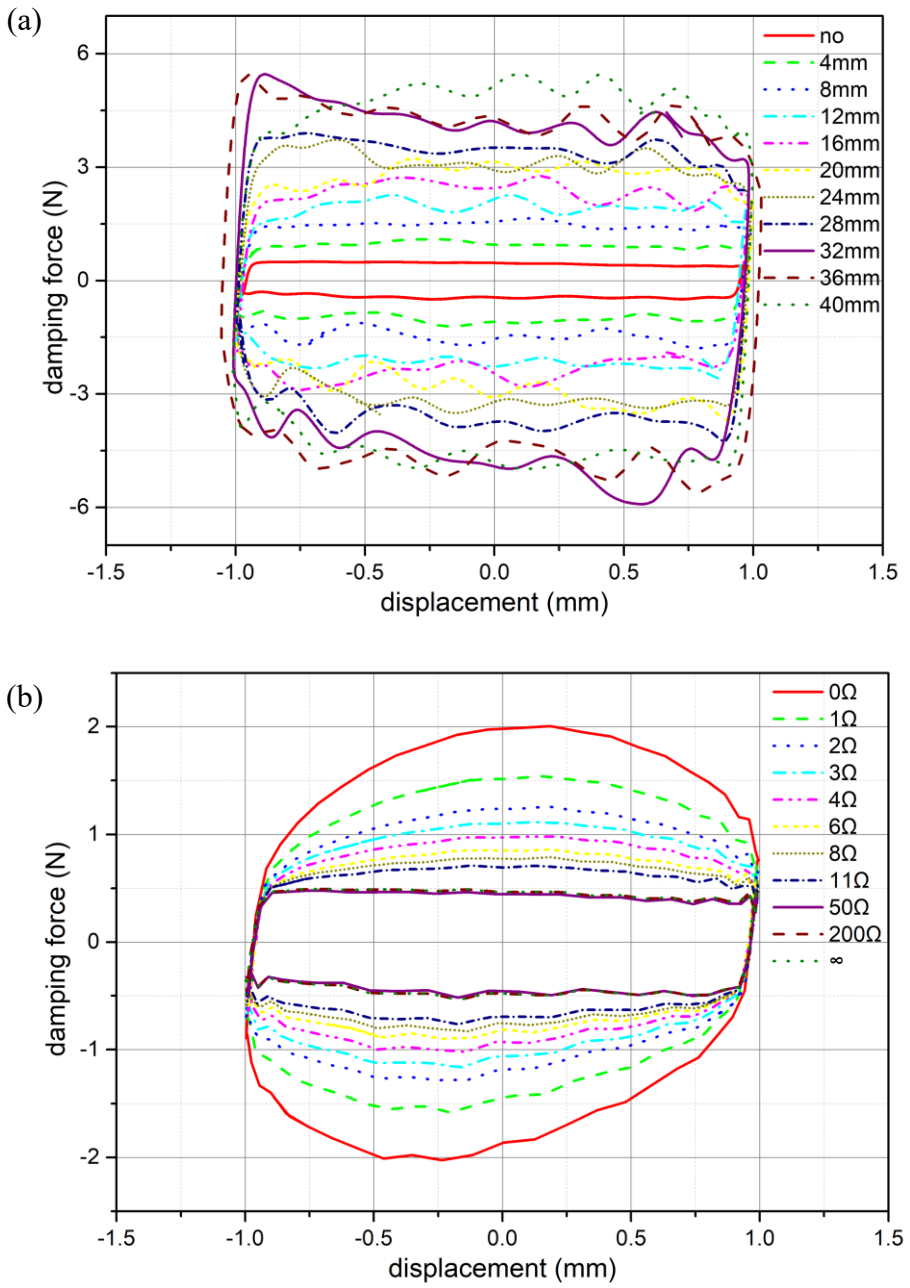

Fig. 10. Hysteresis loop of the proposed hybrid damper: (a) FD hysteresis loop with various deformation lengths of tuning spring (b) EMSD hysteresis loop with various external resistance

The damping force of the FD fluctuates because of the lack of a tightly linear guide when the normal force (indexed by the deformation length of the tuning spring) is getting large. The fluctuation can be reduced or eliminated by fixing the friction pads at the proper location in FD. The introduction of a linear guide is bound to increase the parasitic damping which will affect the damping component analysis. Since the proposed FD and EMSD are combined, the parasitic damping hysteresis loop of the two

dampers have a similar value in Fig. 11 ($c_P \approx 10\mathrm{N}\cdot\mathrm{s/m}$). Moreover, the parasitic damping hysteresis loop is roughly a rectangle, which shows similar property between the parasitic damping and Coulomb damping.

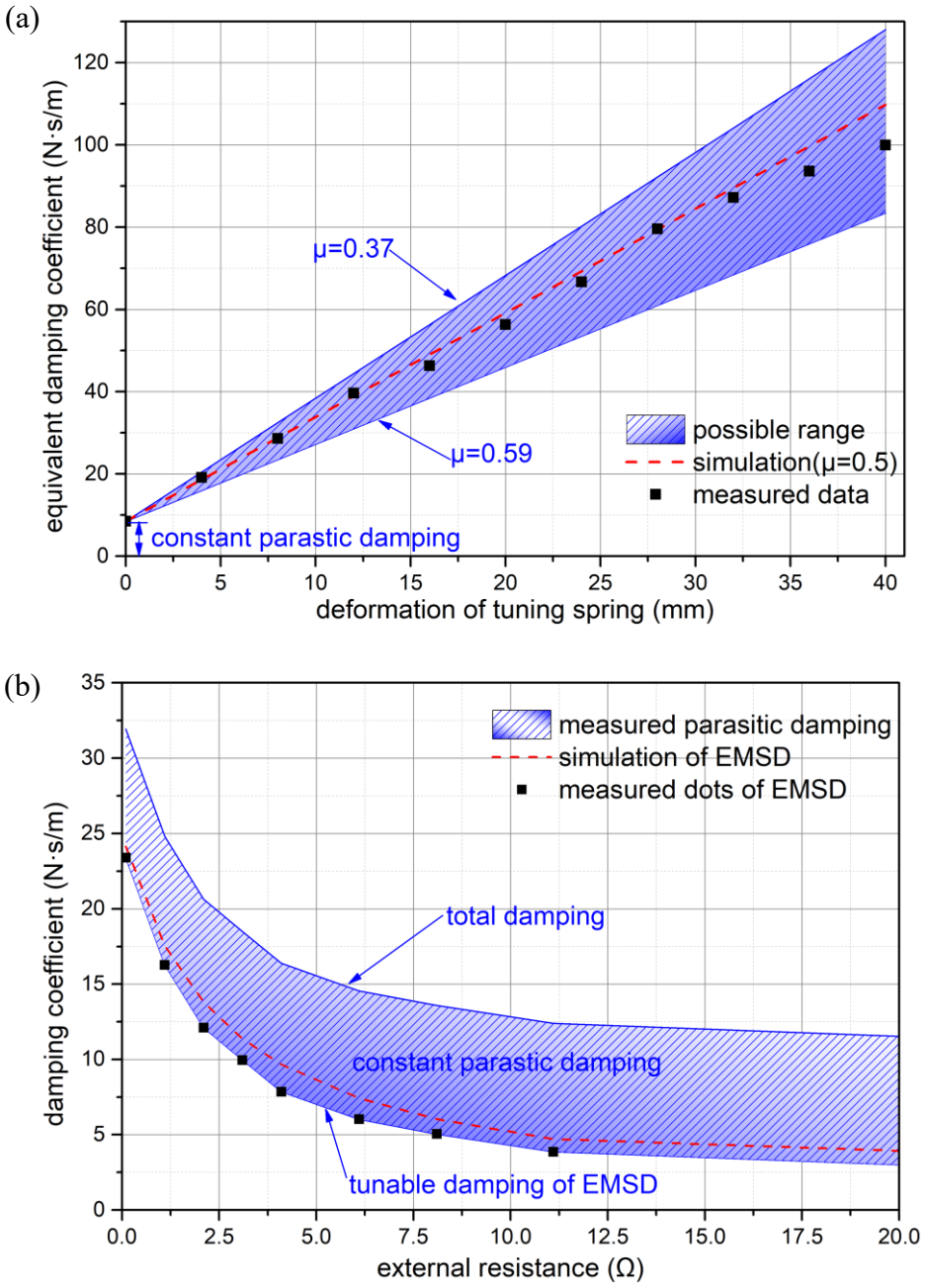

Fig. 11. Measured and simulated damping coefficient variation. (a) FD with different deformations of the tuning spring, (b) EMSD with different external resistance values

The calculated μk_R in Eq.(17) is around 0.125 with the measured damping force and the corresponding Δs in Fig. 10. Subsequently, the corresponding friction coefficient can be calculated as $\mu = 0.51$, which falls into the limited interval $[0.37, 0.59]$. With the obtained friction coefficient, the simulated damping coefficient of the FD can be calculated based on Eq.(16), shown as the red dash line in Fig. 11a

with various deformations of the tuning spring. The measured damping coefficient of FD is shown by the black dot in Fig. 11a by processing the measured hysteresis loop based on Eq.(22). The simulated and measured results of the FD damping coefficient agree well in Fig. 11a, which demonstrates the effectiveness of the proposed FD model.

With the calculated K_t and Z_{in}, the simulated damping coefficients with different external resistance values can be obtained through Eq.(1), drawn as the red dash line in Fig. 11(b). The measured damping coefficient of EMSD is also shown as the black dots in Fig. 11b with the same method of FD as described before. Moreover, both the tunable damping of the EMSD and the total damping with constant parasitic damping with different external resistances are plotted in Fig. 11b. The simulated and measured ESMD damping coefficients match well except that the simulated ones are slightly higher when the external resistance is large. The possible reason is that the parasitic is not measured accurately enough.

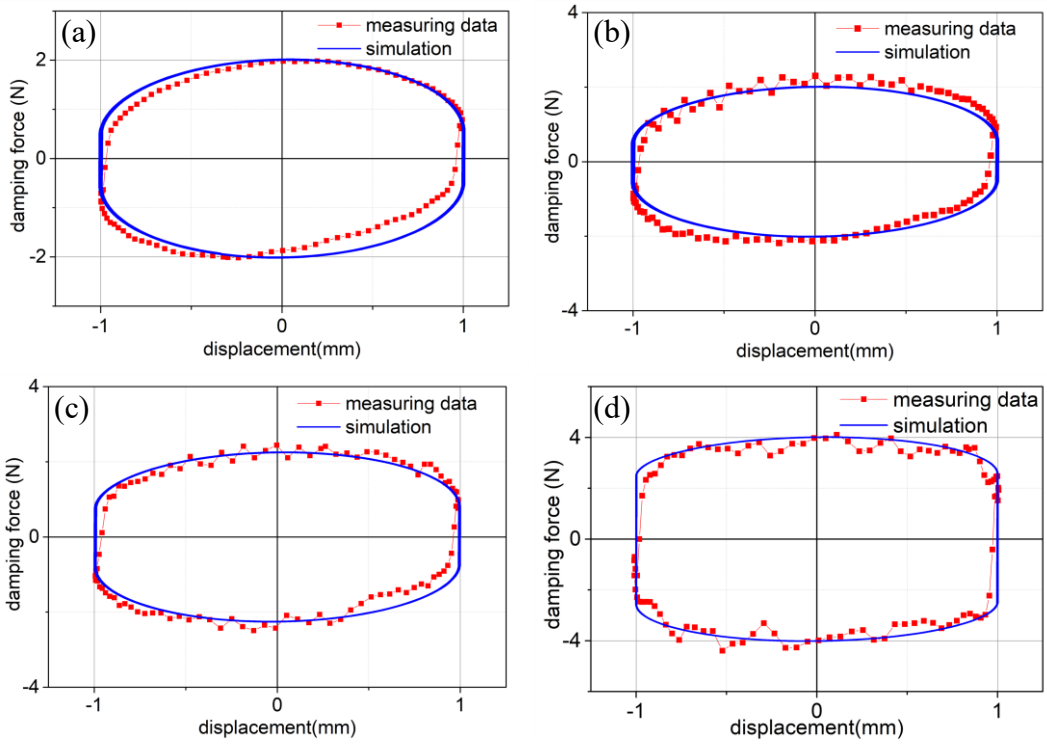

Fig. 12. Hysteretic loop of the proposed tunable hybrid damper: (a) friction blocks disconnected (just parasitic damping and EMSD with zero external resistance), (b) friction blocks connected with zero deformation of the tuning springs, (c) deformation of the tuning spring at 2 mm, (d) deformation of the tuning spring at 16 mm

With the verified damping coefficient calculation method, the measured hysteresis loops of the proposed hybrid damper with tunable Coulomb damping and fixed maximum electromagnetic shunt damping are plotted in Fig. 12 for comparison with the simulated results. Examinations on the four tuning spring scenarios of the FD listed in Fig. 12 show that the measured hybrid damping match well with the simulated results with different normal forces. As supplementary information, more hysteresis loop

comparison figures are provided in Fig. A.1, also evidencing the agreement between the calculated and measured results.

The hysteresis loops of the proposed hybrid damper look similar, but not exactly the same. Based on the quasi-static models and without considering the system parasitic damping, the damping force of the MR damper includes two parts: the viscous damping force and the force due to yield stress of the magnetorheological fluid. Since both forces are related to the magnetic field, the hysteresis loop cannot be described easily. The proposed hybrid damper can be regarded as a combination of a pure viscous damper and a Coulomb friction damper. The hysteresis loop is a simple superposition of rectangle and ellipse. The mechanism of the proposed hybrid damper can then be identified, which is easier than the MR damper.

4. Experimental implementation of the optimum DVA

Upon verifying the proposed hybrid damper model, the following experiments are conducted to investigate the damping tunability of the proposed hybrid damper when it is applied to a DVA system.

4.1 Experiment setup

The proposed hybrid damper is installed in a DVA system, shown in Fig. 13, to calibrate the H_∞ optimal DVA through tunable damping. The experimental system is built up based on the theoretical model in Fig. 5. The proposed hybrid damper with FD and EMSD is installed in the middle part of the system. A tuning mechanism is fixed with the primary system and regarded as an integrated part of the primary system mass, while the moving part is connected with the DVA counter-weight which also contributes to the DVA mass. The natural frequency is tuned to 9Hz by changing the primary mass before the DVA is added to the system. Other parameters are listed in Table 2.

Table 2. Identified parameters of the experimental system

Notation	Values	Description
f_{n1}	9 Hz	Natural frequency of the primary system
f_{n2}	8.1876 Hz	Natural frequency of DVA
γ	0.849	Natural frequency ratio
k_1	20.961 N/mm	Stiffness of primary system
k_2	2.686 N/mm	Stiffness of DVA
m_1	6.5549 kg	Equivalent mass of the primary system
m_2	1.165 kg	Equivalent DVA mass
μ	0.1778	Mass ratio

As shown in Fig. 13, a non-contact electromagnetic exciter mounted on top of the mounting frame provides the excitation force without introducing additional stiffness to the dynamic system. The exciter coil is fixed on the mounting frame while the permanent magnets of the exciter are fixed on the primary system which can be

regarded as part of the primary mass. The linear guide is composed of 4 rotation bearings on each side face, and the smooth glassy surface for bearing motion allows reducing the parasitic damping of the primary system. A force sensor is used on the top of the primary mass to measure the excitation force. Two displacement sensors are used to measure the absolute displacement of the primary system mass and that of the DVA mass. A nylon tube with a pre-compressed DVA spring inside is fixed on the tuning mechanism of the FD to provide a rough linear guide for the DVA mass vibration. Moreover, an 8-bit electromagnetic relay combination is used to control the resistance of the variable resistor.

The data acquisition and signal generation are conducted with the B&K PULSE 7767 system. The driving signal to the exciter is amplified by the B&K 2712 power amplifier before sending it to the non-contact exciter.

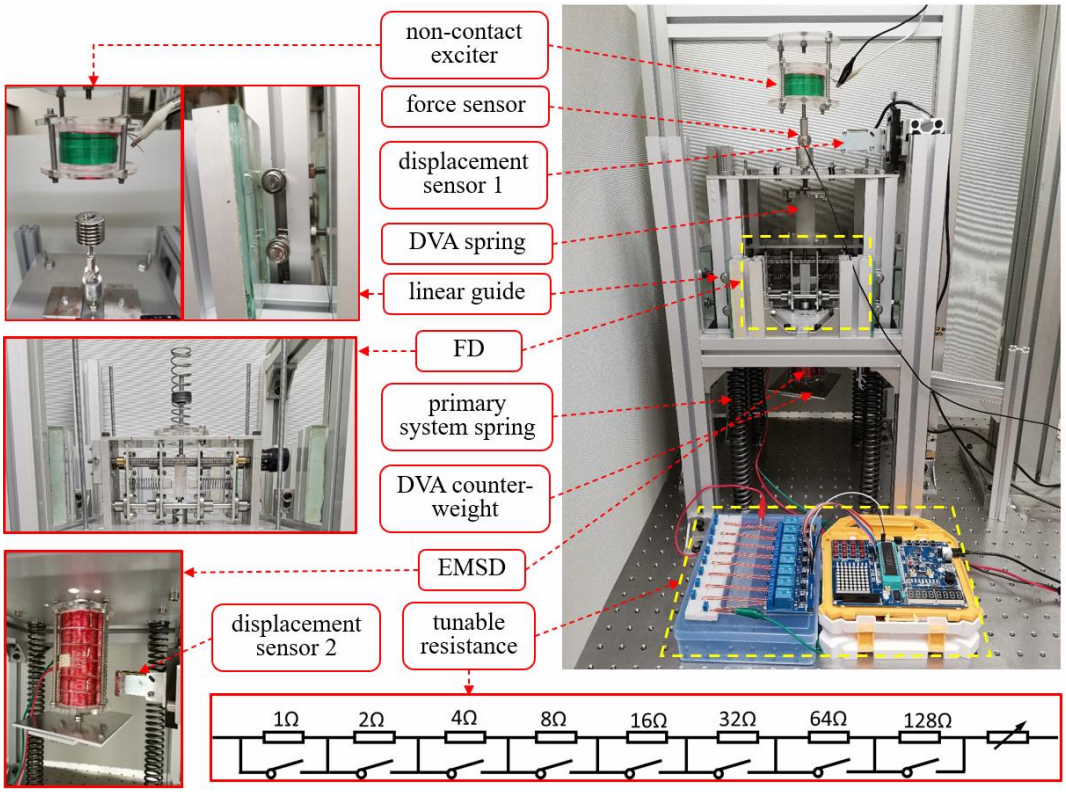

Fig. 13. Experimental set-up of DVA system with a tunable hybrid damper

4.2 Fixed-points calibration

The pre-requisite of the optimum DVA implementation is to tune the natural frequency ratio into the calculated parameters listed in Table 2 based on Eq.(11). However, some parameters (such as the mass of the primary system and that of the DVA) are not able to be quantified precisely, the system calibration can be conducted by tuning the fixed-points into the same value with different damping. With the selected spring of the primary system and DVA, and the natural frequency of the primary system is located at 9Hz, the only changeable parameter with no restriction is the DVA mass for achieving the optimum frequency ratio between the primary and the DVA system. To check whether the dimensionless vibration amplitude X_1/X_{st} of the primary mass m_1

at the fixed-points (P and Q in Fig. 14) is equal or not, the displacement frequency response curves of the primary mass with three different damping values are plotted to find the fixed points. With better damping tunability and sufficient tuning range, the EMSD is utilized for the fixed-points calibration. As shown in Fig. 14, the fixed-points P and Q possess the same dimensionless magnitude with properly tuned DVA.

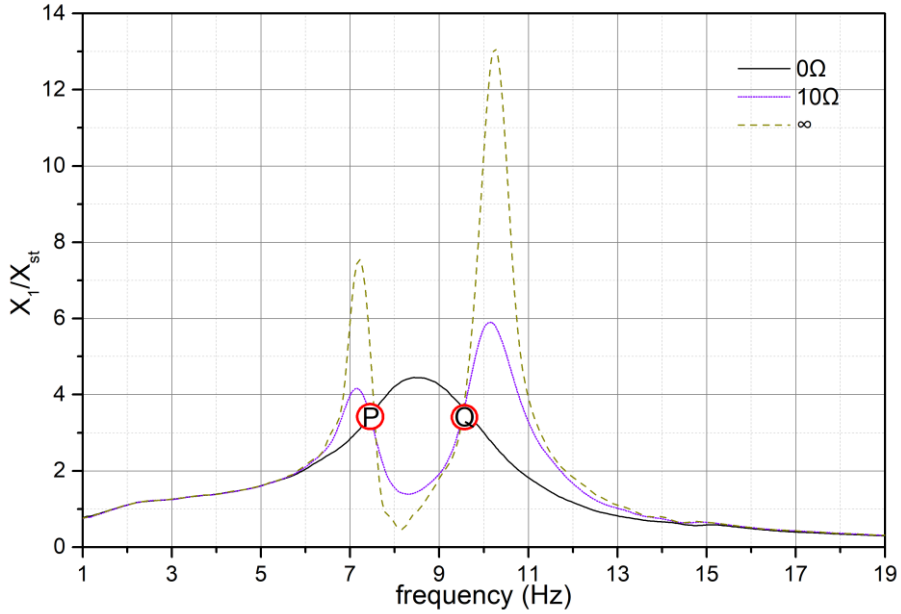

Fig. 14. Fixed points calibration

The next step is to tune the damping of the EMSD such that the fixed points P and Q become the peaks of the frequency response curve. The three curves in Fig. 14 already show that the fixed points P and Q locate at different positions of the curve. With more precise tuning of the EMSD damping, the H_∞ optimal DVA is obtained by locating the maximum response points at the fixed points P and Q in the next section.

4.3 Results analysis

The measured response spectra of mass m_1 with EMSD and FD are shown in Fig. 15. With the fine-tuning of the EMSD damping, the optimal DVA with equal resonant vibration amplitudes is achieved when the external resistance of EMSD equals 3Ω as shown in Fig. 15a. On the other hand, when the deformation length of the tuning spring is about 4 mm, H_∞ optimal tuning of the DVA is experimentally achieved. However, the response magnitude is not able to maintain at exactly the same value near the fixed points with different deformations of the tuning springs, especially with a large damping force. The measurement results verified the conclusions from references [34-36] that the FD functions better when the Coulomb damping force is small relative to the excitation force. Therefore, FD is only suitable to provide coarse tuning of the damping.

To investigate the FD influence on the DVA damping tuning, the response spectra of mass m_1 with the proposed FD and EMSD within the working boundary are

measured and plotted in Fig. 16. Similar results between Fig. 16 and Fig. 15a show that the FD with a small damping force has a slight influence on the stability of the DVA system.

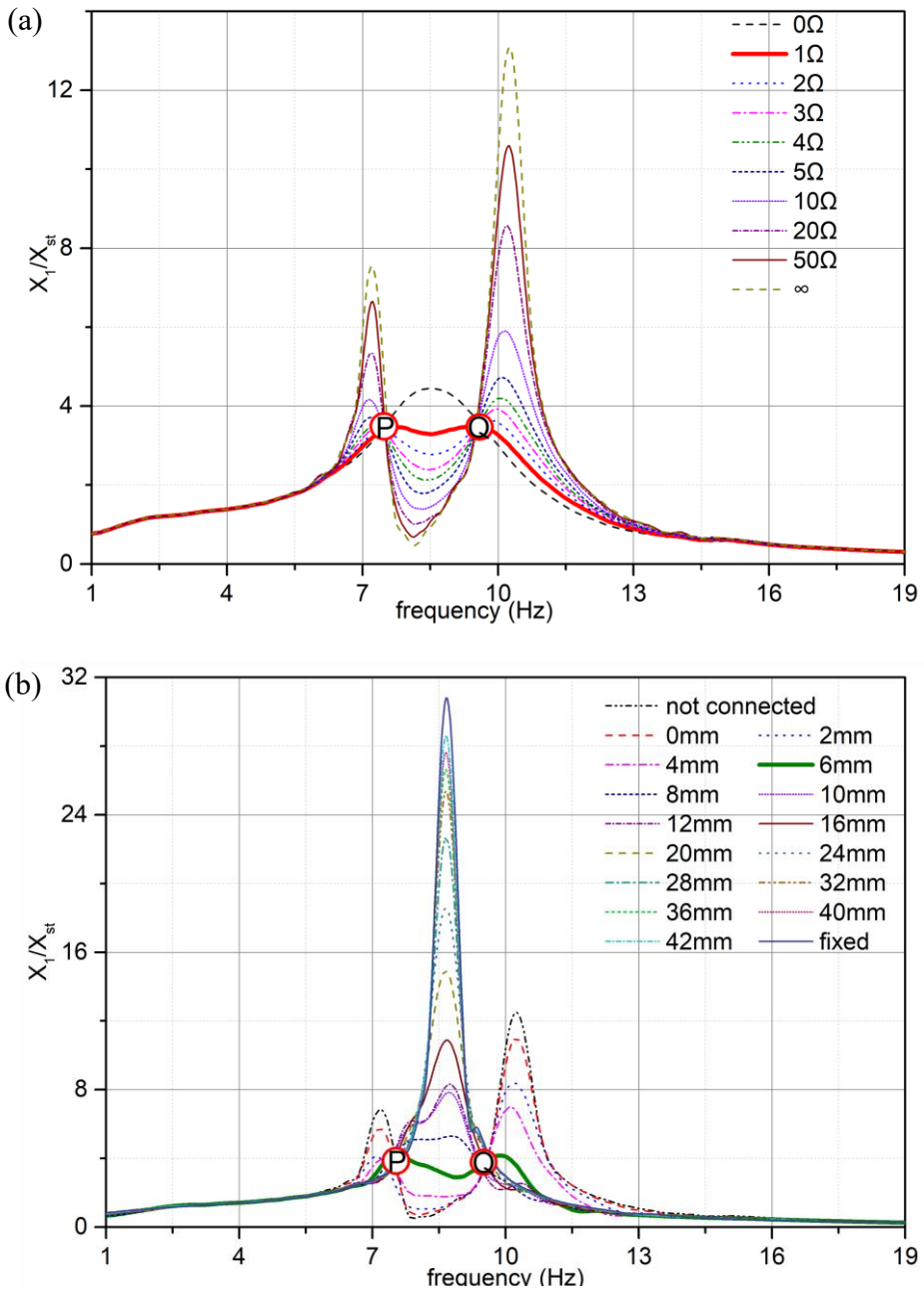

Fig. 15. Primary system response with two kinds of tunable dampers respectively: (a) tunable EMSD with different electrical resistances, (b) tunable FD with different deformations of tuning springs

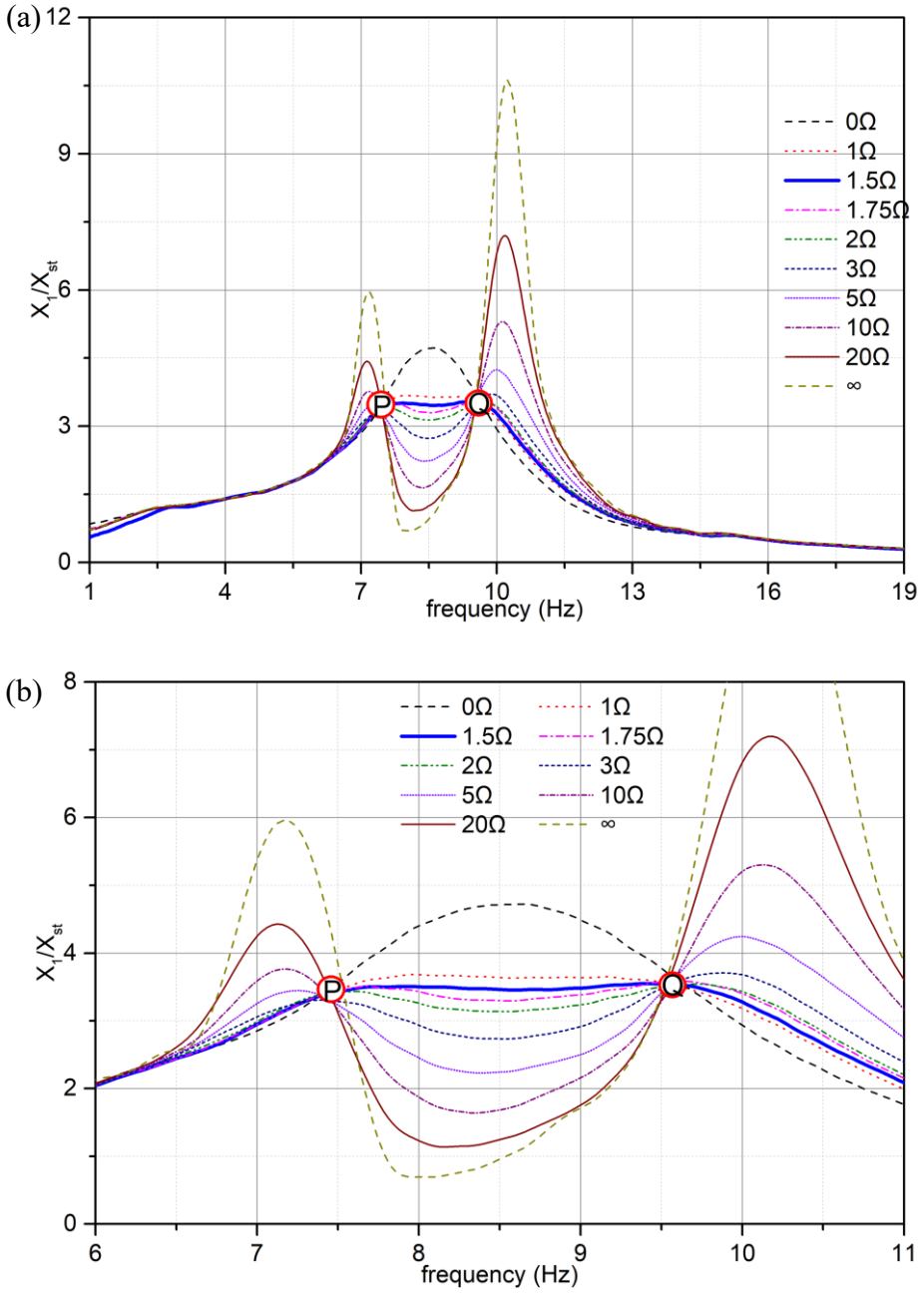

Fig. 16. Primary system response with the proposed hybrid damper when FD friction blocks are just connected and EMSD with different external resistance. (a) response curves in full frequency range, (b) closeup around the fixed-points.

With the verification of tunability of the individual damper as described above, the hybrid damper is used for the H_∞ optimal DVA calibration with both EMSD and FD being activated. The response spectra in Fig. 15b show that the damping force provided by FD is sufficient for the optimal DVA damping requirement when the deformation of the tuning springs is between 4 mm and 6 mm. Therefore, tests on hybrid damper are conducted with the fixed FD when $\Delta s < 4$ mm. The response curves of the primary mass with different Δs of the FD and external resistance of EMSD are plotted in Fig.

17. The required tuning of Δs of the FD and the corresponding external resistance of EMSD for H_∞ optimal DVA obtained from the experiments are listed in Table 3.

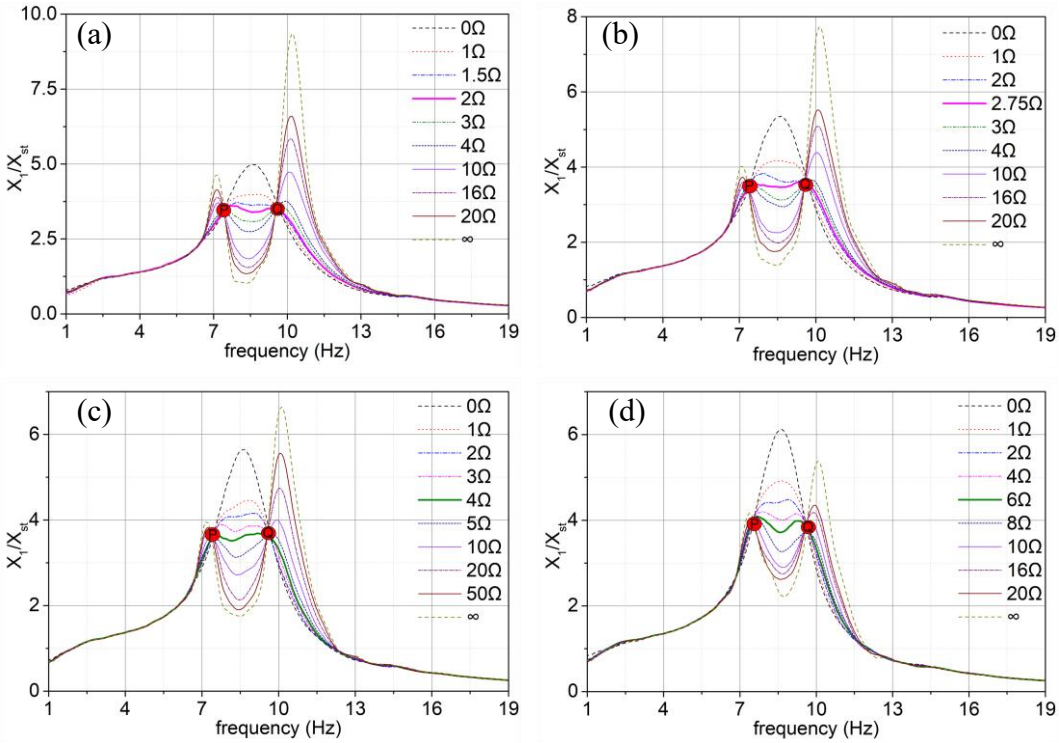

Fig. 17. Primary system response with the proposed hybrid damper when EMSD external resistance varies and FD deformation length of tuning spring are fixed at: (a) 1 mm, (b) 2 mm, (c) 3 mm, (d) 4 mm

The damping adjustment of the proposed hybrid damper shows that FD can be utilized as a coarse tuning damper with the fine-tuning EMSD working together to achieve the optimum DVA. With the increasing deformation length of the FD tuning spring, the EMSD damping required by the H_∞ optimal DVA calls for higher external resistance. Therefore, the coarse damping tuning ability of the FD successfully shifts the EMSD from the sensitive domain into the non-sensitive domain as shown in Fig. 4 to allow more precise tuning of the EMSD.

Table 3. Tuned parameters of hybrid damper for H_∞ optimal DVA

Δs of FD	R_{load} of EMSD
not connected	1 Ω
0mm (just connected)	1.5 Ω
1 mm	2 Ω
2 mm	2.75 Ω
3 mm	4 Ω
4 mm	6 Ω

5. Conclusions

A hybrid damper with tunable Coulomb and electromagnetic shunt damping (EMSD) is proposed to cope with applications requiring damping tunability. The proposed hybrid damper is applied to a DVA and H_∞ optimal damping of the absorber is achieved experimentally. The theoretical model of the hybrid damper with tunable damping is also experimentally verified. Coulomb damping can be adjusted by varying the compressive spring force acting on the friction blocks of the damper. The Coulomb damper is used to provide the coarse tuning of the hybrid damper while the EMSD supplements by offering fine-tuning of the damping to the damper. Both theoretical and experimental analyses show that the Coulomb damper is capable of enlarging the tunable range of the EMSD damping without compromising its tuning accuracy. The tunable EMSD adopts a six opposing magnet pair configuration which has been proved sufficiently effective. The damping provided by the EMSD is adjustable by varying the external electrical resistance of the EMSD circuit. Meanwhile, fine adjustment of the external resistance of the EMSD circuit provides sufficient tunability of the damping force of the damper. The measured damping coefficients match well with the calculated results from the theoretical models of the pure EMSD, FD, and the FD-EMSD hybrid damper. As an application example, the damper is implemented in a DVA which requires a precise tuning of the damping to work at its optimum condition. Experiments show that the H_∞ optimal working condition is readily setup owing to the FD-enabled coarse tuning and EMSD-induced fine-tuning abilities. Meanwhile, theoretical prediction, in terms of lowering the tuning sensitivity of the EMSD by its combined usage with the FD, is also confirmed by experiments.

Acknowledgments

The authors would like to acknowledge the Research Grant Council of Hong Kong for the funding support (Project number: 15206120).

Appendix. Hysteresis loops of the hybrid damper

As a supplement to Fig. 12, the intact hysteresis loops of the proposed hybrid damper are plotted in Fig. A.1. The corresponding deformation of the tuning spring varies with the interval of 2 mm ($\Delta s \leq 8$ mm) or 4mm ($\Delta s > 8$ mm). The model effectiveness of the proposed hybrid damper is verified through the agreement between experimental and simulation results, shown in Fig. A.1.

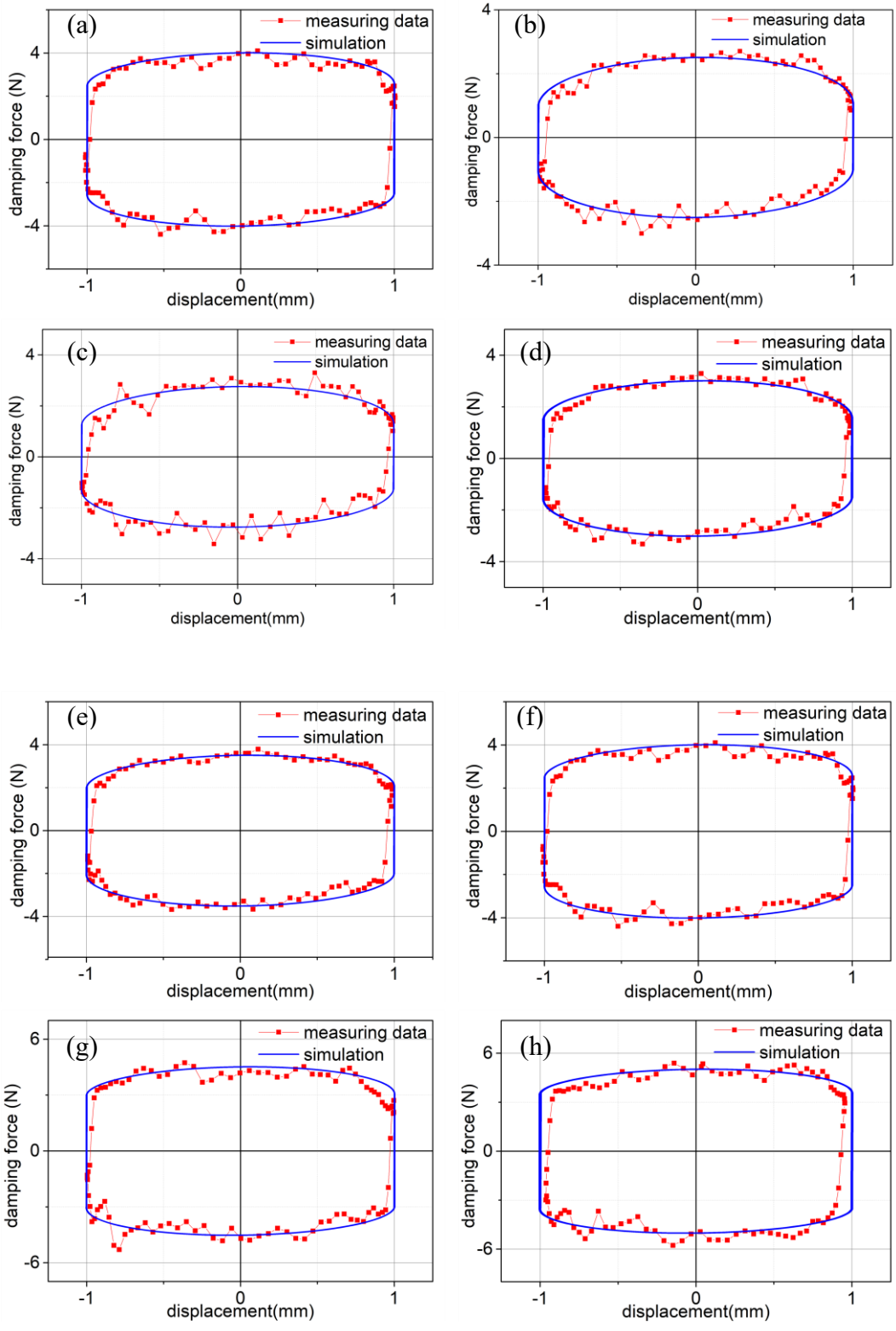
(a)
measuring data
simulation
damping force (N)
displacement(mm)
(b)
measuring data
simulation
damping force (N)
displacement(mm)
(c)
measuring data
simulation
damping force (N)
displacement(mm)
(d)
measuring data
simulation
damping force (N)
displacement(mm)
(e)
measuring data
simulation
damping force (N)
displacement(mm)
(f)
measuring data
simulation
damping force (N)
displacement(mm)
(g)
measuring data
simulation
damping force (N)
displacement(mm)
(h)
measuring data
simulation
damping force (N)
displacement(mm)

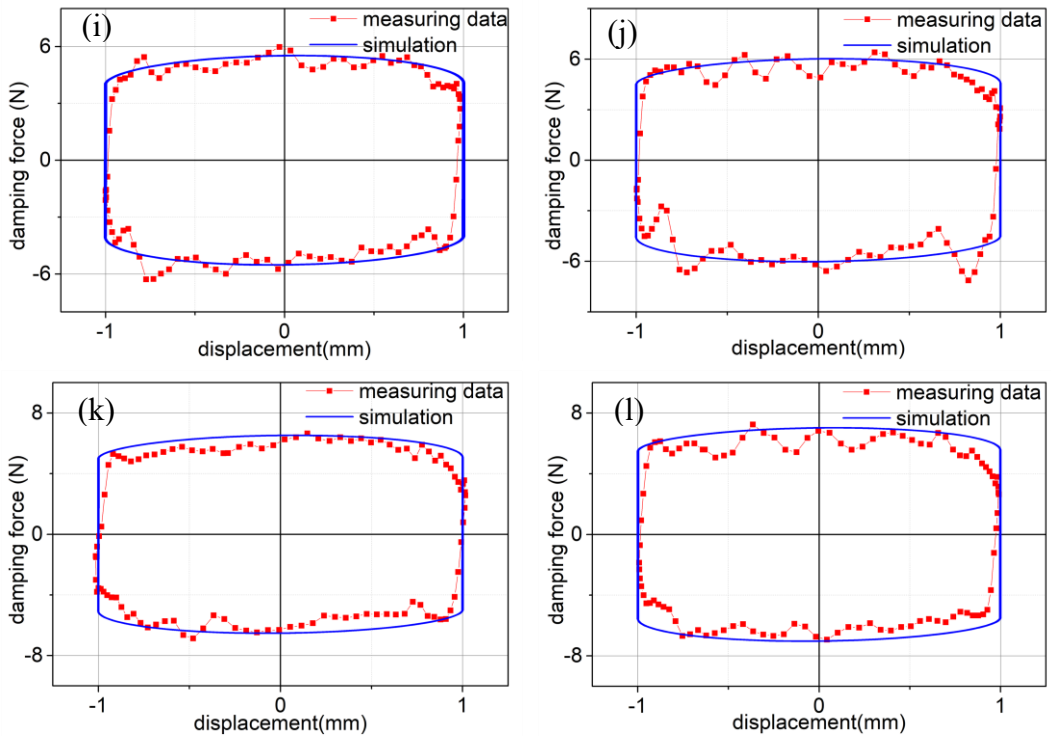

Fig. A.1. Hysteresis loops of the proposed tunable hybrid damper when the deformation of the tuning spring is (a) 2mm, (b) 4mm, (c) 6mm, (d) 8mm, (e) 12mm, (f) 16mm, (g) 20mm, (h) 24mm, (i)28mm, (j) 32mm, (k) 36mm, and (l) 40mm

References

[1] S. Behrens, A.J. Fleming, S.O.R. Moheimani. "Electromagnetic shunt damping." IEEE/ASME International Conference on Advanced Intelligent Mechatronics (AIM 2003). Vol. 2. IEEE, Kobe, Japan, (2003): 1145-1150. https://doi.org/10.1109/AIM.2003.1225504.

[2] S. Behrens, A.J. Fleming, S.O.R. Moheimani. "Vibration isolation using a shunted electromagnetic transducer. " Smart Structures and Materials 2004: Damping and Isolation. Vol. 5386. International Society for Optics and Photonics. San Diego, CA, USA, (2004): 506-515. https://doi.org/10.1117/12.539690.

[3] B. Yan, H. Ma, N. Yu, L. Zhang, C. Wu. "Theoretical modeling and experimental analysis of nonlinear electromagnetic shunt damping." J Sound Vib 471 (2020): 115184. https://doi.org/10.1016/j.jsv.2020.115184.

[4] B. Yan, H. Ma, L. Zhang, C. Wu, X. Zhang. "Electromagnetic shunt damping for shock isolation of nonlinear vibration isolators." J Sound Vib. 479 (2020): 115370. https://doi.org/10.1016/j.jsv.2020.115370.

[5] R. Sun, W. Wong, L. Cheng. "Tunable electromagnetic shunt damper with opposing magnets configuration." Smart Mater Struct. 29.11 (2020): 115034. https://doi.org/10.1088/1361-665X/abb21d.

[6] M. Yuan, K. Liu, A. Sadhu. "Simultaneous vibration suppression and energy harvesting with a non-traditional vibration absorber." J Intel Mat Syst Str. 29.8 (2018): 1748-1763. https://doi.org/10.1177/1045389X17754263.

[7] T. Inoue, Y. Ishida, M. Sumi. "Vibration suppression using electromagnetic resonant shunt damper." J Vib Acoust. 130.4 (2008): 041003. https://doi.org/10.1115/1.2889916.

[8] T. Ikegame, K. Takagi, T. Inoue. "Exact solutions to H∞ and H2 optimizations of passive resonant shunt circuit for electromagnetic or piezoelectric shunt damper." J Vib Acoust. 141.3 (2019): 031015. https://doi.org/10.1115/1.4042819.

[9] S. Zhu, W. Shen, X. Qian. "Dynamic analogy between an electromagnetic shunt damper and a tuned mass damper." Smart Mater Struct. 22.11 (2013): 115018. https://doi.org/10.1088/0964-1726/22/11/115018.

[10] B. Yan, Y. Luo, X. Zhang. "Structural multimode vibration absorbing with electromagnetic shunt damping." J Vib Control. 22.6 (2016): 1604-1617. https://doi.org/10.1177/1077546314543809.

[11] T. Cheng, I. Oh. "Vibration suppression of flexible beam using electromagnetic shunt damper." IEEE T Magn. 45.6 (2009): 2758-2761. https://doi.org/10.1109/TMAG .2009.2020549.

[12] H. Niu, X. Zhang, S. Xie, P. Wang. "A new electromagnetic shunt damping treatment and vibration control of beam structures." Smart Mater Struct. 18.4 (2009): 045009. https://doi.org/10.1088/0964-1726/18/4/045009.

[13] S. Behrens, A.J. Fleming, S.O.R. Moheimani. "Passive vibration control via electromagnetic shunt damping." IEEE-ASME T Mech. 10.1 (2005): 118-122. https://doi.org/10.1109/TMECH.2004.835341.

[14] D. Niederberger, S. Behrens, A.J. Fleming, S.O.R. Moheimani, M. Morari. "Adaptive electromagnetic shunt damping." IEEE-ASME T Mech. 11.1 (2006): 103-108. https://doi.org/10.1109/TMECH.2005.859844.

[15] A. Paknejad, G. Zhao, S. Chesné, A. Deraemaeker, C. Collette. "Hybrid electromagnetic shunt damper for vibration control." J Vib Acoust. 143.2 (2021): 021010. https://doi.org/10.1115/1.4048389.

[16] X. Tang, Y. Liu, W. Cui, L. Zuo. "Analytical solutions to H2 and H∞ optimizations of resonant shunted electromagnetic tuned mass damper and vibration energy harvester." J Vib Acoust. 138.1 (2016): 011018. https://doi.org/10.1115/1.4031823.

[17] W. Ao, P. Reynolds. "Analysis and numerical evaluation of H∞ and H2 optimal design schemes for an electromagnetic shunt damper." J Vib Acoust. 142.2 (2020): 021003. https://doi.org/10.1115/1.4045455.

[18] B. Yan, H. Ma, L. Zhang, W. Zheng, K. Wang, C. Wu. "A bistable vibration isolator with nonlinear electromagnetic shunt damping." Mech Syst Signal Pr. 136 (2020): 106504. https://doi.org/10.1016/j.ymssp.2019.106504.

[19] H. Ma, B. Yan. "Nonlinear damping and mass effects of electromagnetic shunt damping for enhanced nonlinear vibration isolation." Mech Syst Signal Pr. 146 (2021): 107010. https://doi.org/10.1016/j.ymssp.2020.107010.

[20] Bo Yan, Ning Yu, Hongye Ma, Chuanyu Wu. A theory for bistable vibration isolators, Mechanical Systems and Signal Processing, 167(2022): 108507. https://doi.org/10.1016/j.ymssp.2021.108507.

[21] L. Zuo. W. Cui. "Dual-functional energy-harvesting and vibration control: electromagnetic resonant shunt series tuned mass dampers." J Vib Acoust. 135.5 (2013): 051018. https://doi.org/10.1115/1.4024095.

[22] Y. Pei, , Y. Liu, L. Zuo. "Multi-resonant electromagnetic shunt in base isolation for vibration damping and energy harvesting." J Sound Vib. 423 (2018): 1-17. https://doi.org/10.1016/j.jsv.2018.02.041.

[23] F. M. Foong, , C. K. Thein, D. Yurchenko. "Important considerations in optimising the structural aspect of a SDOF electromagnetic vibration energy harvester." J Sound Vib. 482 (2020): 115470. https://doi.org/10.1016/j.jsv.2020.115470.

[24] Q. Cai, S. Zhu. "Enhancing the performance of electromagnetic damper cum energy harvester using microcontroller: concept and experiment validation." Mech Syst Signal Pr. 134 (2019): 106339. https://doi.org/10.1016/j.ymssp.2019.106339.

[25] S. Zhou, C. Jean-Mistral, S. Chesné. "Electromagnetic shunt damping with negative impedances: optimization and analysis." J Sound Vib. 445 (2019): 188-203. https://doi.org/10.1016/j.jsv.2019.01.014.

[26] A. Stabile, G.S. Aglietti, G. Richardson, G. Smet. "Design and verification of a negative resistance electromagnetic shunt damper for spacecraft micro-vibration." J Sound Vib. 386 (2017): 38-49. https://doi.org/10.1016/j.jsv.2016.09.024.

[27] B. Yan, X. Zhang, H. Niu. "Design and test of a novel isolator with negative resistance electromagnetic shunt damping." Smart Mater Struct. 21.3 (2012): 035003. http://dx.doi.org/10.1088/0964-1726/21/3/035003.

[28] J.P. Den Hartog. "Forced vibrations with combined viscous and Coulomb damping." Phil. Mag. 9.59 (1930): 801-817. https://doi.org/10.1080/14786443008565051.

[29] L. Marino, A. Cicirello, D.A. Hills. "Displacement transmissibility of a Coulomb friction oscillator subject to joined base-wall motion." Nonlinear Dynam. 98.4 (2019): 2595-2612. https://doi.org/10.1007/s11071-019-04983-x.

[30] L. Marino, A.Cicirello. "Experimental investigation of a single-degree-of-freedom system with Coulomb friction." NONLINEAR DYNAM. 99.3 (2020): 1781-1799. https://doi.org/10.1007/s11071-019-05443-2.

[31] E. Guglielmino, T. Sireteanu, C.W. Stammers, G. Ghita, M. Giuclea. "Semi-active suspension control: improved vehicle ride and road friendliness." Springer Science & Business Media, (2008). https://doi.org/10.1007/978-1-84800-231-9.

[32] F. Weber, J. Høgsberg, S. Krenk. "Optimal tuning of amplitude proportional Coulomb friction damper for maximum cable damping." J Struct Eng. 136.2 (2010): 123-134. https://doi.org/10.1061/(ASCE)0733-9445(2010)136:2(123).

[33] J.P. Den Hartog. "Mechanical Vibrations." Dover publications, Inc. New York,

(1985): 79-117.

[34] A. Hartung, H. Schmieg, P. Vielsack. "Passive vibration absorber with dry friction." Arch Appl Mech. 71.6 (2001): 463-472. https://doi.org/10.1007/s004190000149.

[35] B.J. Vidmar, B.F. Feeny, S.W. Shaw, A.G. Haddow, B.K. Geist, N.J. Verhanovitz. "The effects of Coulomb friction on the performance of centrifugal pendulum vibration absorbers." Nonlinear Dynam. 69.1 (2012): 589-600. https://doi.org/10.1007/s11071-011-0289-7.

[36] J. Fang, Q. Wang, S. Wang, Q. Wang. "Min-max criterion to the optimal design of vibration absorber in a system with Coulomb friction and viscous damping." Nonlinear Dynam. 70.1 (2012): 393-400. https://doi.org/10.1007/s11071-012-0462-7.

[37] G. Zeng, B. Basu. "A study on friction-tuned mass damper: harmonic solution and statistical linearization." J Vib Control. 17.5 (2011): 721-731. https://doi.org/10.1177/1077546309354967.

[38] A. Sinha, K.T. Trikutam. "Optimal vibration absorber with a friction damper." J Vib Acoust. 140.2 (2018): 021015. https://doi.org/10.1115/1.4038272.

[39] D. Cree, M. Pugh. "Dry wear and friction properties of an A356/SiC foam interpenetrating phase composite." Wear. 272.1 (2011): 88-96. https://doi.org/10.1016/j.wear.2011.07.008.